ADVANCED MATERIALS INTERFACES
www.advmatinterfaces.de

Thin Film NCM Cathodes as Model Systems to Assess the Influence of Coating Layers on the Electrochemical Performance of Lithium Ion Batteries

*Hendrik Hemmelmann, Julius K. Dinter, and Matthias T. Elm**

A facile procedure is demonstrated to prepare lithium nickel cobalt manganese oxide (NCM) thin film cathodes. Via a sol-gel approach and subsequent spin-coating, a crystalline and phase-pure cathode layer is prepared without any further additives or binders. It is shown that the thin film cathodes are ideal model systems to access the effect of coating layers on electrochemical performance in lithium ion batteries. For this purpose, the thin films are coated with an ultrathin alumina layer using atomic layer deposition. The samples are structurally and electrochemically characterized, exhibiting comparable properties as cathodes prepared from powder. After cycling, post-mortem analysis is conducted to investigate structural changes inflicted by the electrochemical treatment. The characterization reveals that uncoated samples exhibit severe structural changes due to cycling, while coated samples show only minor changes under the same conditions. Post-mortem surface analysis using X-ray photoelectron spectroscopy confirms the corrosion of the uncoated cathode and proofs the scavenging effect of alumina. The presented results provide a simple and versatile method to prepare thin film NCM model systems, which enable an accurate analysis of the cathode–electrolyte interface and thus allow to obtain a deeper understanding of the beneficial effect of coatings for next-generation lithium ion batteries.

1. Introduction

The need for energy storage materials has drastically increased over the last decades. Especially with the rising interest in mobile electronic devices, smart consumer products, and electromobility, the research on battery materials gained huge momentum in recent years.[1–4] Most of the mobile electronic devices would not be possible without the lithium ion battery (LIB), which was commercially released by SONY in 1991. With its high capacity of around 160 mAh g^{-1}, good rate capability, and cycling performance, lithium cobalt oxide (LCO) became the prototype of modern cathode materials in lithium ion batteries.[5] In the following years, cobalt was more and more substituted by manganese, aluminium and/or nickel due to its high costs.[6] The most promising group of these substitution materials are the lithium nickel cobalt manganese oxides (NCM). They combine the positive aspects of all three oxides (good rate capability, high capacity, and good stability) and are in the focus of intense research.[7] Combined with lithiated graphite as anode and a liquid electrolyte, they became state-of-the-art examples for modern, mobile battery systems.

However, there are still negative aspects with this class of material, such as side reactions occurring at both the anode and the cathode during intercalation and deintercalation of lithium ions. During cycling, degradation of the organic electrolyte compounds forms a so called solid electrolyte interface (SEI).[8–11] On the anode side, this layer leads to a decrease in performance. Regardless of the downside, the SEI on the anode benefits the cycling stability in the long run due to the formation of a passivating layer that hinders further corrosion and side reactions. On the cathode side, however, the side reactions not only degrade the electrolyte but also the active material itself leading to the formation of a cathode-electrolyte interface (CEI), which impedes lithium ion transport at the surface.[12–15] During cycling, the NCM gets delithiated, which destabilizes the cathode material due to the lithium loss in the structure. Consequently, transition metals get dissolved into the electrolyte, especially manganese, which is known to dissolve in organic solvents. Another source for corrosive specimens is $LiPF_6$, the

H. Hemmelmann, J. K. Dinter, Dr. M. T. Elm
Center for Materials Research
Justus-Liebig-University Gießen
Heinrich-Buff-Ring 16, 35392 Gießen, Germany
E-mail: Matthias.elm@phys.chemie.uni-giessen.de
Dr. M. T. Elm
Institute of Physical Chemistry
Justus-Liebig-University Gießen
Heinrich-Buff-Ring 17, 35392 Gießen, Germany
Dr. M. T. Elm
Institute of Experimental Physics I
Justus-Liebig-University Gießen
Heinrich-Buff-Ring 16, 35392 Gießen, Germany
The ORCID identification number(s) for the author(s) of this article can be found under https://doi.org/10.1002/admi.202002074.

DOI: 10.1002/admi.202002074

conductive additive in the electrolyte. With the residual water inside the electrolyte or water generated by the decomposition of organic molecules, $LiPF_6$ decomposes and thereby produces HF.[16,17] The acid dissolves the transition metals and the lithium ions on the NCM surface, producing again water and HF during this process, and thus creating a degradation spiral, which leads to significant capacity fading.[12,17–19]

There are various approaches in literature that deal with this issue, like doping the cathode material with stabilizing ions like Ti^{4+}, Zr^{4+}, or Mg^{2+} or using alternative conductive salts (e.g., $LiClO_4$, LiBOB) in the liquid electrolyte.[20–22] Another promising method to prevent the degradation of the cathode surface is coating the cathode material with a nanometer thin coating layer to create an artificial CEI.[23–25] While at first, the overall resistance of the cell increases, the performance can be stabilized at high efficiencies in the long time run.[26] The coating acts as a blocking layer, preventing direct contact between the cathode surface and the electrolyte species and therefore alleviates unwanted side reactions like corrosion of the cathode, dissolution of metals into the electrolyte, or unwanted phase transitions. The downside, however, is that the coating increases the cell resistance and acts as a barrier which needs to be overcome by the Li^+ ions during cycling.[27–30] Many different coatings are recently being discussed in literature, ranging from Li^+ ion conducting materials like $LiNbO_2$ to insulating and chemically inert materials like Al_2O_3 or MgO. All of these materials improve the cycling stability and the overall electrochemical performance.[31–33]

However, the exact mechanisms of the reactions occurring at the surface and in the protective layer (transport through coating, side reactions etc.) are not well understood yet. Thus, a more detailed analysis of the reaction products formed at the surface of coated and uncoated cathodes is desirable in order to design effective coatings with optimized properties. Unfortunately, the spherical nature of the secondary particles typically used as active material in the cathode prohibits a proper surface analysis. To utilize analytical methods like X-ray photoelectron spectroscopy (XPS), atomic force microscopy (AFM), or time-of-flight secondary ion mass spectrometry (ToF-SIMS) with a high surface sensitivity and a maximum efficiency, 2D model systems (thin film battery electrodes) are needed.[34] In recent years, this topic became more and more important in the battery community all over the world. While the deposition of LCO thin films is known for many years, there are not many publications regarding the successful deposition of NCM thin films.[35–38] Most of the research on NCM thin films focuses on physical vapour deposition (PVD) methods like sputtering or pulsed laser deposition (PLD).[34,39–41] Thus, the deposition of these films requires high vacuum conditions and a huge amount of energy for the deposition process. Furthermore, the films often grow epitaxially with a preferred orientation, which does not reflect the structural properties of cathodes commercially used in LIBs.

Here, we present a facile and reproducible way to synthesize NCM thin film cathodes by a sol-gel process using spin coating. The thin films exhibit a smooth surface and a randomly distributed orientation of the crystallites making them an ideal model system, which allows not only to determine the intrinsic properties of cathode materials, such as the lithium diffusion coefficient, but also enables a detailed study of the electrode–electrolyte interface properties before and after cycling using surface sensitive techniques.[42] To assess the suitability of the thin films to serve as model electrodes, the influence of a protective coating on their electrochemical performance was investigated. For this purpose, some thin films were coated with an ultra-thin Al_2O_3 protective layer using atomic layer deposition (ALD). Electrochemical cycling and cyclic voltammetry were performed subsequently on pristine and coated cathode thin films. To get a better insight on the comparability to powder samples and into structural changes of the thin films inflicted by the electrochemical treatment, a thorough structural analysis on the pristine and Al_2O_3 coated cathodes before and after electrochemical cycling was performed. Post-mortem analysis of the cycled and washed thin films enabled a first look on the surface reactions prohibited by the protective coating. AFM measurements confirm the structural degradation of the pristine sample, while XPS analysis reveals that the Al_2O_3 coating scavenges the corrosive fluorine species to bind it, creating a passivation layer at the interface. Furthermore, the formation of NiF_2 and MnF_2 species at the interface was confirmed using XPS, whose signals are usually superimposed by signals of the additives used in powder-based electrodes. Overall, we show that the thin films acts as a suitable and adaptable model system for NCM cathode materials, which offer a detailed investigation of the formation, the composition, and the structural properties of the CEI without interference of binders or additives.

2. Results and Discussion

2.1. Analysis of the Protective Al_2O_3 Coating Layer

In order to confirm the successful deposition of the ultrathin Al_2O_3 coating layer on top of the cathode, the characteristic Al 2p and Ni $2p_{3/2}$ signals of different coating thicknesses of 2 nm and 5 nm were measured using XPS as a function of sputter etching time. The results are shown in **Figure 1**. For the pristine thin films, a strong Ni $2p_{3/2}$ signal can be detected at 855.2 eV, which is in good agreement with values reported in literature for Ni^{2+} in NCM.[14,43,44] A weak Al 2p signal at around 74.2 eV is visible, which disappears with increasing etching time (Figure 1d). We therefore attribute this to a small amount of surface contamination.

For both coated samples, a strong Al 2p signal at around 74.4 eV is visible (Figure 1e,f), which shifts to lower binding energies during the first sputtering step. According to Maibach et al. this effect is related to the calibration on the C1s adventitious carbon species.[45] Due to surface effects, the binding energies of this carbon species shift and therefore alter the position of other surface species when calibrated to the C1s signal. After removing this surface species and getting a constant signal for all species, the binding energy of the cleaned Al_2O_3 surfaces are 74.3 eV and 74.8 eV for the thin films coated with a 2 nm and 5 nm thin Al_2O_3 layer, respectively. These values are in good agreement with literature values for Al_2O_3.[46,47] Further sputtering leads to a decrease in the Al 2p signal intensity in both cases while the intensity of the Ni $2p_{3/2}$ signal and its satellite signals arise (Figure 1b,c). The energetic position of the Ni $2p_{3/2}$ signal at about 855.1 eV is again in good agreement with literature data of NCM.[9,48,49] For the surface of a sample

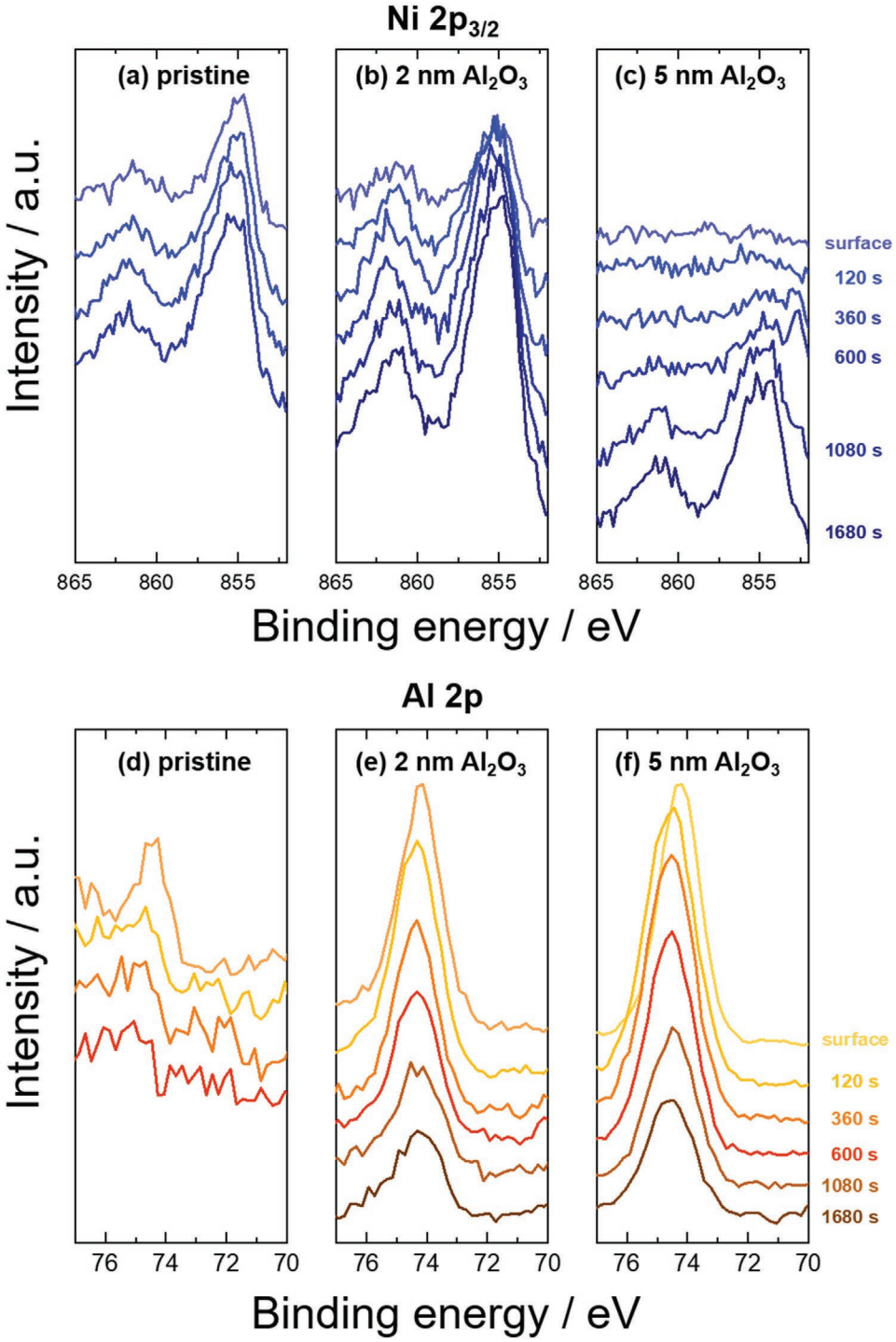

Figure 1. XPS analysis of a,d) the pristine thin film and the thin films coated with b,e) 2 nm and c,f) 5 nm alumina.

coated with a 5 nm thin layer of alumina and even after the first two sputter steps, no Ni 2p signals are measurable. It is worth noting that XPS is a surface sensitive method with a typical maximum analysis depth of 3–7 nm. However, the actual analysis depth depends on the material itself and initial and final state processes. The absence of a Ni 2p signal in case of the coated NCM thus shows a very high sensitivity to the first few nanometers of the surface and confirms a complete and homogeneous coating of the thin films. In the case of the 2 nm coated sample (Figure 1b), the Ni 2p is observed even without a sputtering step, revealing that the coating layer is sufficiently thin, so that the photoelectrons of the NCM material can reach the analyser. We expect the ALD growth process to be the same for both layer thicknesses and therefore assume that the 2 nm

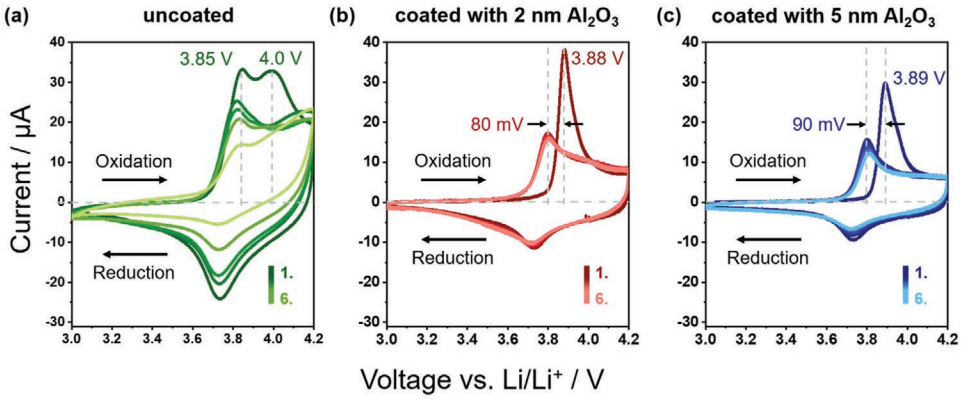

Figure 2. CV curves of a) the pristine NCM film and the NCM thin films coated with b) 2 nm and c) 5 nm alumina.

coated sample also exhibits a homogeneous Al_2O_3 coating of the surface. Overall, the XPS results indicate a successful coating of the NCM thin film cathodes.

2.2. Electrochemical Analysis of NCM Thin Films Coated with Al_2O_3

Electrochemical cycling of the pristine and coated thin film cathodes were performed against a metallic lithium anode using 1 M $LiPF_6$ in EC:DMC (1:1) as electrolyte. Cyclic voltammograms of the first six scans of the pristine and coated NCM thin films are shown in **Figure 2**. All CV curves show the typical oxidation (3.8 V) and reduction peaks (3.7 V) in a voltage range between 3.0 and 4.2 V, which are attributed to the Ni^{2+}/Ni^{4+} redox couple of NCM111.[43] For the uncoated sample shown in Figure 2a, the main oxidation peak during the first scan is shifted to a slightly higher potential (3.85 V), which is known to occur in NCM powder-based cells as well.[50] However, more prominent is a second peak occurring in the anodic scan at around 4 V. Interestingly for the coated samples (Figure 2b,c) this peak is barely visible or completely vanishes. The origin of this peak at around 4 V may be attributed to reactions on the surface of the cathode material which no longer occur when the surface is coated with an inert material. In literature there are several explanations, which reaction may be responsible for the presence of the second oxidation peak. According to Chen et al. the peak at 4 V can be attributed to an additional phase transition during oxidation of NCM811. The first transition from the hexagonal layered phase to a monoclinic one is located at around 3.8 V, while the second transition, from the monoclinic to a second hexagonal phase, occurs at around 4.0 V.[51] This behaviour is also found for NCM111 powder materials.[51] Several studies confirm that an ultrathin coating of the cathode material inhibits the additional phase transition at around 4.0 V, which is in good agreement with our findings.[52–54] Another possibility for the second oxidation peak in the CV of the uncoated thin films is the decomposition of the electrolyte happening at the surface. This would also explain why the corresponding peak is missing in the cathodic scan. In the cathodic scan, only one reduction peak at 3.73 V (lithiation) occurs. In combination with the oxidation peak visible at around 3.85 V (delithiation), these two peaks correspond to the Ni^{2+}/Ni^{4+} redox pair. In the second cycle, the oxidation peak of NCM is located at 3.81 V and therefore shifts to a lower voltage by 40 mV. This behaviour is typically observed during the first and second cycles of NCM. According to Kasnatscheew et al. the increase of the cell resistance in the first cycle can be explained by parasitic surface reactions, like electrolyte decomposition, but also by structural changes in the cathode material.[55] With increasing cycling numbers, the oxidation peak starts to shift again to higher potentials by about 20–30 mV during the first five charge–discharge cycles, indicating an increase in the cell resistance and therefore implying the formation of a passivation layer on the surface of the cathode. During the first cathodic scan, a shift of roughly 10 mV to lower potentials is also visible for the reduction peak, starting at 3.73 V during the first scan. Consequently, the overpotential of the cell increases by roughly 40 mV during the first five charge–discharge cycles. During the first cycles, the current decreases significantly, starting with an oxidation peak current of 33 µA during the first cycle and dropping to 9 µA during the fifth cycle. The decrease in current with each cycle is accompanied by a loss in capacity, further indicating the formation of a decomposition layer.

The cathode thin film coated with 2 nm Al_2O_3 (Figure 2b) shows a sharp and prominent peak at 3.88 V in the first anodic scan which indicates a significant higher overpotential compared to the uncoated samples, where the peak is located at 3.85 V during the first cycle. The high overpotential of 80 mV is attributed to the higher resistance arising from the delithiated Al_2O_3 coating layer as lithium needs to diffuse through the coating layer into the electrolyte during charging. However, as for the uncoated sample, the peak shifts to lower potentials (3.8 V) for the subsequent cycles indicating the lithiation of the Al_2O_3 coating accompanied with an improved conductivity for Li^+. For the subsequent anodic scans, a nearly identical behavior with an oxidation peak occurring at approximately 3.8 V is found. The same holds for the cathodic part, which reaches a maximum at 3.73 V. Minor polarisation during subsequent cycling indicates only a minimal increase in the cell resistance. As shown in Figure 2c, a comparable behavior is also found for the cathode thin film coated with a 5 nm thin Al_2O_3 surface layer. The first anodic peak reaches its maximum at 3.89 V, that is, at a slightly higher overpotential of 90 mV. The even higher overpotential is mainly attributed to the higher resistance of the thicker coating layer. However, as for the 2 nm coated cell, the anodic peak of the second cycle exhibits

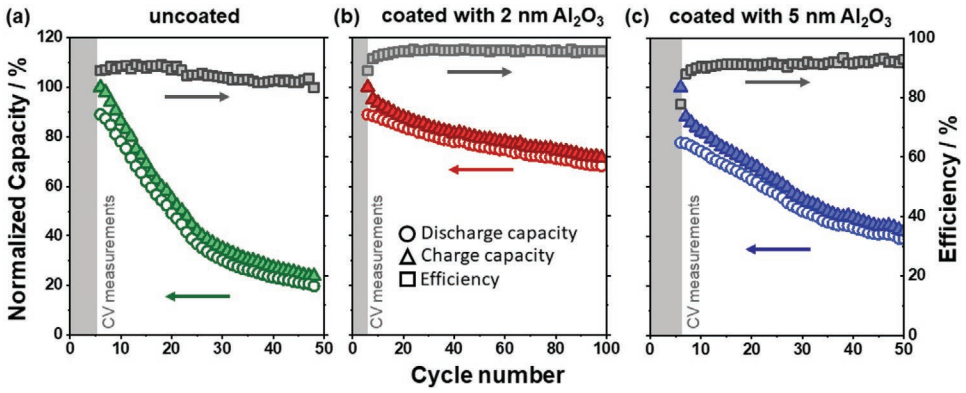

Figure 3. a) Cycling performance tests of a pristine NCM film (green) b) a sample coated with 2 nm (red), and c) 5 nm (blue) alumina after CV measurement. The coulombic efficiency of each cell is displayed in grey. Voltage profiles can be found in Figure S1, Supporting Information.

its maximum at 3.8 V, while for the following cycles, the peak shifts to a slightly higher potential of 3.81 V. This corresponds to the shift of the reduction peak from 3.73 to 3.72 V observed of the cathodic scan during the first six cycles. In both coated thin films, there are minor to no traces of a second oxidation peak around 4.0 V as observed for the uncoated thin film cathode. As mentioned before, this oxidation peak is attributed to surface reactions and/or to an additional phase transition of the active material, which are hindered by the coating with alumina. After the CV measurements, the cycling stability of the thin films were measured at a rate of 0.1 C in a potential window between 3.0 and 4.2 V as shown in **Figure 3**. The thin films exhibit capacity values of about 60–80 mAh g^{-1}, which is significantly lower compared to powder NCM cathodes typically showing capacities in the range of 160–170 mAh g^{-1}.[56] The reason is that the NCM thin films possess a lower electrochemical active surface area compared to powder materials and contain no additional additives. Comparable results were also reported by Philipp et al. who investigated the electrochemical properties of sputtered NCM thin films.[41] Furthermore, it has to be noted that the electrochemical cycling of the cathodes was preceded by a cyclic voltammetry (CV) analysis (grey region in Figure 3), resulting in differences in the initial capacity of the first cycling after the CV measurements. Thus, for better comparison of the cycling behaviour, Figure 3 shows the normalized capacity of each cell. For the pristine NCM thin films (Figure 3a), a significant capacity fading is observed. During the first 20 cycles after the CV measurement, the capacity significantly decreases and reaches only 36.5% of the initial capacity, while the overall efficiency remains constant at about 89%. During the 42nd cycle, the cell further drops to about 23 % of the capacity of the first cycle, and finally breaks down in the consecutive charging step. For the thin film cathode coated with 5 nm alumina, a comparable behavior is observed in the first cycles as shown in Figure 3c. However, the capacity fading during cycling is less pronounced and it retains roughly 50 % of its initial discharge capacity up to the 50th cycle. In contrast, the thin film cathode with 2 nm alumina coating (Figure 3b) shows a significantly higher discharge capacity in the beginning of the cycling procedure. Furthermore, the capacity fading is even more suppressed as the thin film reaches 75 % after the 100th cycle. The efficiency of the cathode coated with 2 nm Al_2O_3, which reaches values of around 97%, also exceeds the efficiency of the 5 nm coated thin film (≈92%). These results confirm the beneficial effect of the alumina coating on the electrochemical performance and indicate that an optimized coating thickness is also crucial for improving cycling stability and rate capability in agreement with results reported for powder samples.[57,58] The decay of capacity is also evident in the rising polarisation with increasing cycling number (Figure S1, Supporting Information) as discussed above.

The beneficial effect of the coating on the long term cycling is also reflected in the cell resistance, which was estimated from the CV as shown in Figure S2, Supporting Information. While the overall cell resistance of the uncoated sample increases rapidly during cycling, a strong increase of the resistance occurs only during the first cycle due to the Al_2O_3 coating. In the subsequent cycles, the increase in resistance is less pronounced also confirming the suppression of undesired surface reactions. The resistance of the thin film coated with 5 nm Al_2O_3 also rises sharply during the first cycle followed by a linear increase with a larger slope than the 2 nm coated sample as also evident in the cycling data (Figure 3). In agreement with the CV data shown in Figure 2, these results clearly demonstrate that coating with an ultrathin layer of alumina improves the cell performance up to a critical layer thickness in accordance with results from powder-based cathodes reported in literature.[59] The comparably low increase of the polarization during cycling in case of the coated samples also shows only minor CEI formation and therefore only a minor increase of the overall cell resistance.

2.3. Structural Characterization of NCM Thin Films Before and After Electrochemical Treatment

To correlate the electrochemical performance with the structural changes of the cathode material, a thorough structural analysis of uncoated and coated cathode thin films was conducted. To enable a direct comparison of the structural properties after cycling, pristine and coated cathodes were disconnected and disassembled after 25 cycles at a discharge state of 3 V. Subsequently, the cathode thin films were rinsed multiple times with electrolyte solution (EC:DMC 1:1) to clean it

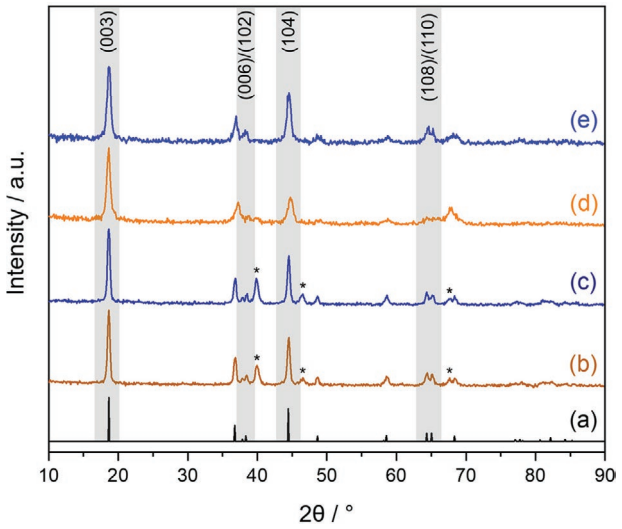

Figure 4. Comparison of the X-ray patterns of spin-coated NCM thin films before and after electrochemical cycling. a) Reference for NCM111 (black, PDF code: 98 015 7146) b) Uncoated and c) coated (5 nm Al_2O_3) NCM thin films before electrochemical cycling. d) Uncoated and e) coated (5 nm Al_2O_3) NCM thin films after electrochemical cycling. Additional reflections (*) arise from the underlying Pt layer.

from residual conductive salt and separator parts. As no significant difference in their structural properties was observed for the thin films coated with 2 and 5 nm alumina, only the sample coated with 5 nm alumina will be discussed in the following. Exemplary results of the cathode coated with 2 nm Al_2O_3 are shown in Figure S3, Supporting Information. **Figure 4** displays the XRD patterns of the pristine thin film and the thin film cathode coated with 5 nm Al_2O_3 before and after electrochemical treatment, respectively. For all four samples, the diffraction lines corresponding to the rhombohedral α-$NaFeO_2$ crystal system with the *R3m* space group are visible. All additional reflections can be attributed to the underlying platinum layer, which functions as current collector. While the patterns of the as-prepared samples are nearly identical independent of the coating layer, differences in shape and intensities of the prominent reflexes are found after the electrochemical treatment. In case of the uncoated thin films the intensity of the (104) reflex after cycling is reduced compared to the prominent (003) reflex. Furthermore, both the (006)/(102) and the (108)/(110) doublets disappear. In case of the coated thin film deterioration of the (006)/(102) doublet is also observable after cycling, however, the (108) and (110) reflexes are still distinguishable. According to literature it is possible to estimate the degree of ordering of the layered structure by the degree of splitting of the (006)/(102) and the (108)/(110) doublets.[60] The clear splitting of the doublets in the uncycled samples (b,c) indicates a good hexagonal ordering of the layered structure in both cases, which is of significant importance for use as a cathode material.[44,60,61] In case of the coated thin film (e) the degree of splitting deteriorates after cycling, indicating a loss of ordering, whereas the uncoated and cycled cathode (d) seems to have lost it completely.

To further investigate the changes of the structural properties during electrochemical treatment, Raman spectroscopy

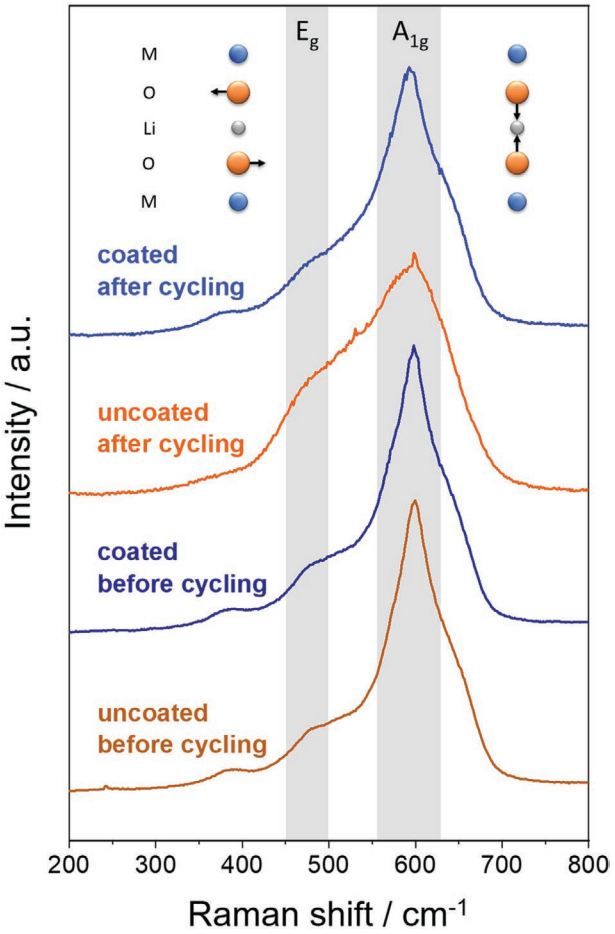

Figure 5. Raman spectra of uncoated and coated (5 nm Al_2O_3) NCM thin film cathodes before and after electrochemical cycling. The characteristic E_g and A_{1g} modes are marked in grey.

of the coated and uncoated thin film cathodes was performed before and after electrochemical cycling. The Raman spectra of all thin films analyzed are shown in **Figure 5**. For all thin film cathodes, two broad bands are visible, the A_{1g} band at about 600 cm^{-1} corresponding to in-plane vibrations δ(O−M−O) and the E_g band at about 480 cm^{-1} corresponding to out-of-plane vibrations of the MO_6 polyhedra.[62] A sharp deconvolution, like for LCO, of the two bands is difficult as the spectrum of NCM is generated by overlapping bands at 474 cm^{-1}, 554 cm^{-1} (Ni−O), 594 cm^{-1} (Mn−O), 486 cm^{-1}, and 596 cm^{-1} (Co−O) of the different vibrations of the transition metal oxygen bonds within the hexagonal lattice.[63,64] The presence of bands other than the E_g and A_{1g} bands may indicate a lower local symmetry potentially arising from complex (Ni/Co/Mn)−O bonding or modes stemming from Mn−O interactions (e.g., the mode around 630 cm^{-1}).[62,65] The E_g and A_{1g} bands further confirm the successful synthesis of phase-pure crystalline material. Comparing the Raman spectra of the uncoated and coated thin films before cycling, no signature of the coating is detectable indicating that the Al_2O_3 coating is too thin to be detected and/or amorphous. However, after cycling, the Raman spectra of the uncoated thin film exhibits differences compared to the spectrum of the coated one. While the intensity ratio of the E_g and

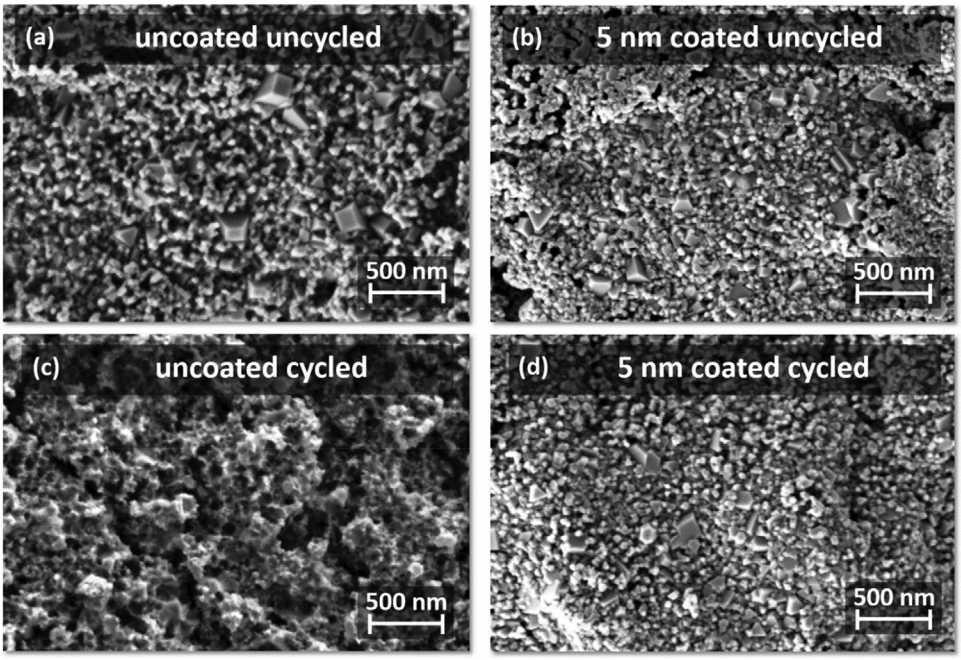

Figure 6. HRSEM images of the surface of an a) uncoated and b) 5 nm coated NCM thin film before cycling. The c) uncoated and d) coated thin films after cycling.

the A_{1g} mode of the coated thin films after cycling is comparable to the ratio before cycling, the A_{1g} mode of the uncoated thin film is significantly attenuated compared to its uncycled counterpart. Thus, the Raman measurements also support the loss of ordering in the structure as already confirmed by the GIXRD measurements. This reduced ordering is another indicator for the decaying capacity within the uncoated sample.

Figure 6 shows the HRSEM images of the uncoated and coated thin films before and after electrochemical cycling. As seen in Figure 6a, the pristine NCM thin film exhibits a homogenous distribution of crystallites on the surface with diameters ranging between 90 and 550 nm. Some of these crystallites seem to be sintered together while other appear to lie loosely on the surface. Most of the crystallites have a cuboctahedrons or cuboctahedron-like shape, exposing different crystal facets at their surfaces. While most of the crystallites are comparable in size and shape, some are elongated or flattened. EDX measurements confirm a homogenous distribution of the transition metals and the expected stoichiometry of $LiNi_{0.33}Co_{0.33}Mn_{0.33}O_2$. There is no evidence of cluster formation of certain elements (Figure S4, Supporting Information). As shown in Figure 6b, coating of the thin film with Al_2O_3 using ALD does not change the surface morphology. This is expected as ALD is well known as deposition technique, which allows the deposition of uniformal and homogeneous coatings with a precise control of the layer thickness even in case of porous thin films.[66–68] After cycling, the coated NCM thin film (Figure 6d) shows no significant difference compared to the pristine sample, while for the uncoated thin film (Figure 6c), changes of the surface morphology are clearly visible. Cracks formed at the surface and it appears as if the particles on the surface became porous. All in all the surface looked damaged, most likely due to corrosion reactions as mentioned before. As the coated thin film shows no changes in surface morphology, reactions causing structural changes seem to be prohibited by the coating layer (Figure 6d). No cracks are visible on the big crystallites that would indicate a swelling and shrinking due to the cycling treatment. Overall, the coating is beneficial for the structural integrity of the thin film during cycling and hinders the degradation of the cathode material.

The surface properties of the thin films were additionally investigated using AFM, as shown in **Figure 7**. In agreement with the results obtained using HRSEM, the AFM measurements reveal that the ALD coating of the thin films does not change the surface morphology significantly. The surface roughness of the uncoated (Figure 7a) thin film cathode is in a range between 26 and 30 nm while for the Al_2O_3 coated thin film cathode (Figure 7b), a comparable roughness of 24 to 29 nm is determined. Filling of small interparticular gaps during the ALD deposition process explains the minor deviation. However, one can clearly identify the crystallites already observed in the SEM pictures. After cycling, AFM measurements further clearly support that the surface topography changes significantly for the sample without the Al_2O_3 protective layer. As shown in Figure 7c, the uncoated thin film after cycling has a rough and bulky surface with maximum height deviations of around 1.6 µm (note here the difference in the scale for Figure 7c compared to the other AFM images) and exhibits an increased surface roughness of 88 to 95 nm. For the coated and cycled thin film shown in Figure 7d, only a minor increase of the surface roughness is detected (25 to 32 nm). This roughening is probably caused by partial corrosion of the top layer of the coating due to the HF stemming from the electrolyte. Except for the as-prepared cathode thin film after cycling, the roughness of all samples are in a comparable range as other thin film cathodes deposited with PVD methods (10–60 nm).[69]

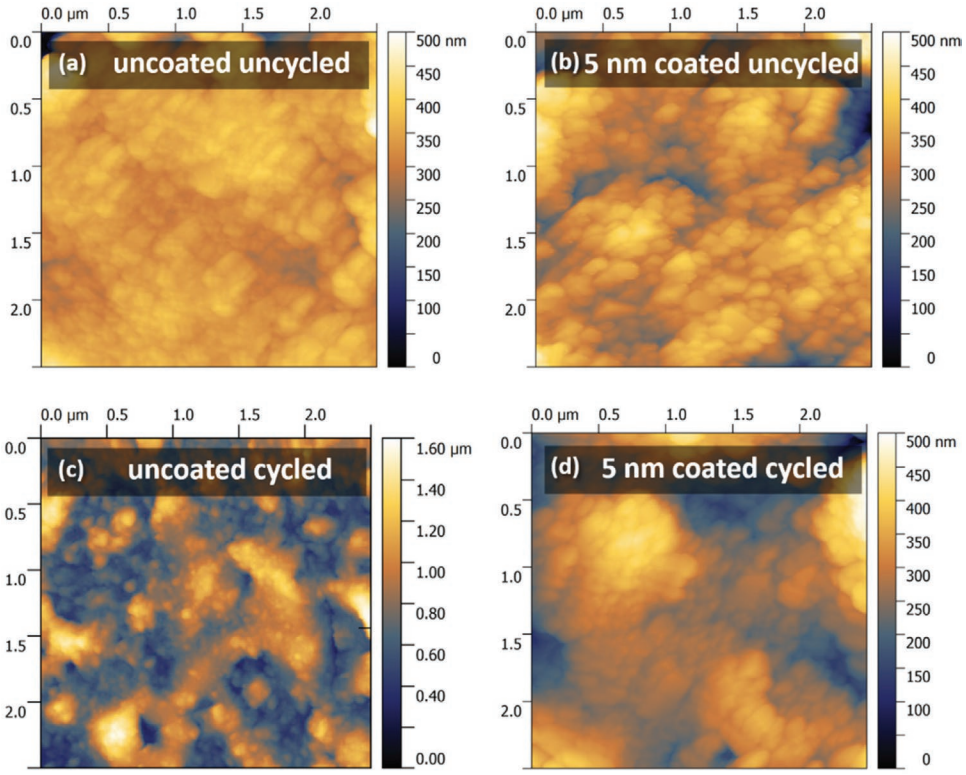

Figure 7. Topographic analysis of an a) uncoated and b) a 5 nm Al_2O_3 coated NCM thin film before cycling and of c) uncoated and d) an Al_2O_3 coated NCM thin film after cycling using AFM.

Xia et al. postulates that a rougher surface is beneficial for the cycling behaviour due to a larger electrochemical active surface in contact with the electrolyte.[70]

2.4. Post-Mortem XPS Analysis of the Coated and Uncoated Cycled Samples

To investigate the beneficial effect of the coating layer in more detail, post-mortem XPS analysis of the uncoated and coated cathode surface was performed after electrochemical cycling. As a first insight into the surface properties of the thin film cathodes after cycling, the F1s XPS signal of the uncoated and coated cathodes were investigated as shown in **Figure 8**. It is worth noting here, that since neither binder like polyvinylidenfluorid (PVDF) nor other additives were used for the electrode preparation, it is possible to analyse the reaction products of the decomposition reaction between the electrolyte and the cathode active material without the influence of carbon additives or binder.

Figure 8a displays the F1s signal of the uncoated sample, which exhibits two prominent peaks at 685.0 eV (orange) and 687.7 eV (blue). Further deconvolution reveals another species at around 686.2 eV (green). The species at around 685.0 eV (orange) is typically associated with LiF.[71–73] A closer look at the missing signal in the Li1s region (inset in Figure 8a) however contradicts the presence of LiF on the surface. It is more likely that this peak originates from a NiF_2-species with a binding energy of around 685.1 eV.[73,74] The binding energy of around 686.2 eV (green) is addressed to MnF_2 species which are typically centred at around 686.1 eV.[75,76] The third resolved peak, identified at around 687.7 eV (blue), is attributed in literature to the formation of either Li_xPF_y, $Li_xPF_yO_z$ or fluorinated carbon species which are typically observed in a similar range and therefore hard to distinguish.[9,19,77] All these results confirm the degradation of the electrolyte, followed by the corrosion of the cathodes surface due to HF which is evident due to the presence of the MnF_2 and NiF_2 species.[78] For the thin films coated with 2 nm (Figure 8b) and 5 nm Al_2O_3 (Figure 8c), the peak at 685.0 eV (orange) is also visible but both samples exhibit a shoulder which can be fitted by a species centred at around 686.9 eV (grey). In case of the coated thin films, the orange peak can be attributed to the binding energy of fluorine in LiF since there is a clear signal in the associated Li spectrum (insets in Figure 8b,c).[34–36] The second peak found at ≈ 686.9 eV (grey) is addressed to the binding energy of AlF_3 (686.5 eV).[73]

Our XPS analysis reveals the benefit of using a binder and additive free 2D cathode model system compared to typical powder-based cathodes. Most powder-based systems need conductive additives and binders like PVDF to become electrochemically cyclable. The signals of PVDF contributing to the F1s spectrum in the XPS analysis overshadow the metal fluoride species like NiF_2 or MnF_2 and thus, making a proper analysis of these fluoride species nearly impossible.[9,14] As LiF is expected to be found in the cathode–electrolyte interface (CEI) of a LIB at 685.0 eV, XPS signals originating from metal fluoride species such as NiF_2 or MnF_2 may be attributed to LiF by

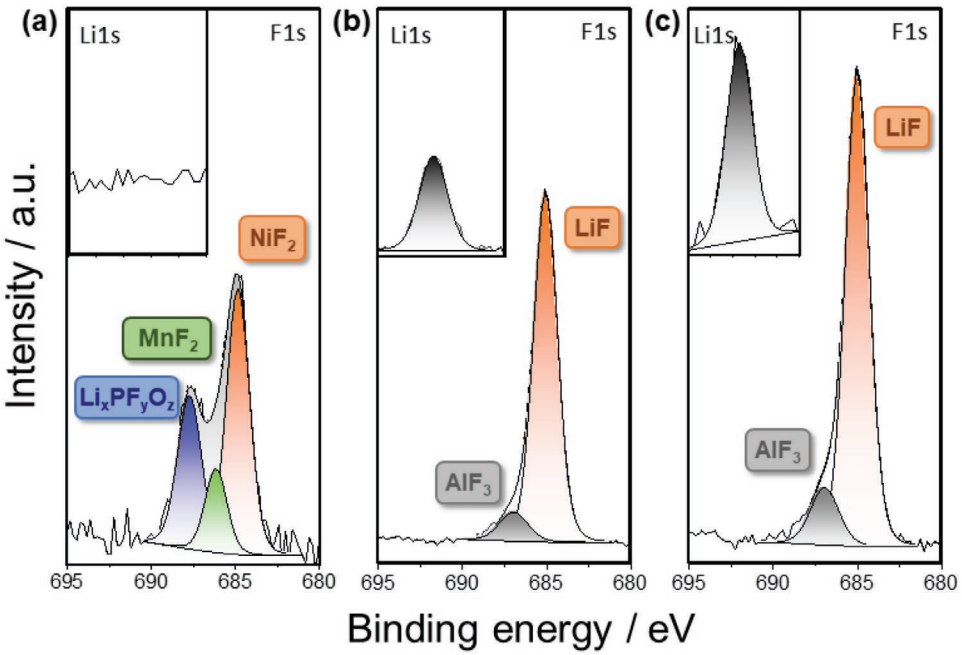

Figure 8. Post-mortem XPS analysis of cycled NCM thin film cathodes a) without coating and films coated with b) 2 nm and c) 5 nm alumina. For better visualization, the spectrum of the uncoated sample was 3x magnified.

mistake, without verifying the existence of the corresponding Li1s signal. Furthermore, with our model system, we could prove that cations are not only dissolved into the electrolyte, which is widely known in literature,[10,18,79–81] but also that the corrosion products are incorporated into the CEI. This offers the possibility to analyse the corrosion products even after washing the cathode with EC:DMC (1:1) to remove residuals from the electrolyte or separator.

In case of the alumina coated samples, the absence of a PVDF signal makes it easier to spot the fluoride species bound to aluminium as a clear shoulder in the overall F1s signal. Martens et al. did a similar analysis on powder samples, showing the difficulties in analysing the F1s spectrum when working with PVDF.[82] The fluorination of the Al_2O_3 observed in the XPS analysis is in good agreement with literature where it is known that an ultrathin alumina layer scavenges the corrosive fluorine species, protecting the cathode underneath.[53,54,59] Additionally, the XPS results confirm that the coating layer prevents the decomposition of the cathode active material as evident by the absence of the XPS signals corresponding to MF_n (M = Ni, Mn) species. It also seems that the alumina layer prevents the incorporation of Li_xPF_y or $Li_xPF_yO_z$ into the CEI as there are also no signals of those species evident. The increased formation of LiF is also related to the protective coating with Al_2O_3. In a recent study, the group of Jeff Dahn proposes a spontaneous reaction of the hexafluorophosphate (PF_6^-) species when it is getting in contact with the oxide coating of cathode materials:[83]

$$2Al_2O_3 + 3PF_{6(solv)}^- \rightarrow 4AlF_3 + 3PO_2F_{2(solv)}^- \quad (1)$$

The as-produced $LiPO_2F_2$ is well known in literature to promote the lifetime and cycling stability of $LiPF_6$ liquid electrolyte based battery cells,[84–86] and it is responsible for the formation of LiF on the cathodes surface as observed for the coated thin films shown in Figure 8.[87]

3. Conclusions

In this paper, we present a versatile solution-based synthesis route to prepare thin film NCM111 cathodes via spin-coating deposition. The as-prepared films are phase-pure and exhibit a crystalline structure comparable to powder NCM. The smooth surface with a roughness of about 20–30 nm allows a detailed analysis of the composition and the morphology of the electrode–electrolyte interface before and after cycling using surface sensitive techniques like XPS and AFM. Also, the beneficial effect of an alumina coating of a few nanometers' thickness on electrochemical performance of NCM cathode materials is observed. While the as-prepared thin films show a poor cycling stability accompanied with side reactions related to the surface, the electrochemical performance was significantly improved by the coated layer. A thorough structural analysis on the pristine and Al_2O_3 coated cathodes before and after electrochemical cycling reveal that the coated cathodes exhibit only minor structural changes after cycling compared to their uncycled counterparts in agreement with results from powder-based electrodes. Only in case of the uncoated cathodes, changes of the crystal structure occur during cycling as confirmed by GIXRD and Raman spectroscopy. Furthermore, HRSEM and AFM investigations reveal that the uncoated thin films suffer from corrosion and mechanical damaging due to crack formation and an increase in surface roughness. Post-mortem analysis of the cathode-electrolyte interface using XPS confirms the degradation of the cathode by the presence of characteristic NiF and

MnF signals. In contrast, only signals originating from LiF and AlF species are found for the coated thin film cathodes. This confirms that the coating scavenges the fluorine species and hinders structural degradation of the cathode. Thus, our results demonstrate the successful deposition of NCM thin film cathodes, which act as a suitable model systems to characterize the interphase properties, interfacial reactions, as well as degradation mechanisms between NCM active material and liquid electrolyte using surface-sensitive techniques such as XPS and AFM. In future, in situ measurements are conceivable, which will enable a direct investigation of the formation of the cathode–electrolyte interface during electrochemical cycling.

4. Experimental Section

Preparation of the Precursor Solution: The precursor solution for the spin coating process was prepared by dissolving stoichiometric amounts of lithium nitrate ($LiNO_3 \cdot H_2O$, 99.99 %), nickel (II) nitrate hexahydrate ($Ni(NO_3)_2 \cdot 6\ H_2O$, 99.999 %), cobalt (II) nitrate hexahydrate ($Co(NO_3)_2 \cdot 6\ H_2O$, 99.999 %), and manganese (II) nitrate tetrahydrate ($Mn(NO_3)_2 \cdot 4\ H_2O$, 99.99 %) in a mixed solvent of deionized water (0.5 mL) and ethanol (3.5 mL). The high amount of ethanol increases the wettability of the substrate during spin coating while water increases the solubility of the compounds. 2.25 mmol of each transition metal nitrate and 2.5 mmol of lithium nitrate were added to the solvent mixture and kept stirring for 10 min. The 10% higher amount of lithium was used to compensate for lithium losses during the heat treatment steps. Subsequently, 150 mg of polyvinylpyrrolidone (PVP, average molecular weight of 40 000) was added to increase the viscosity of the solution. All chemicals were purchased from Sigma–Aldrich. The as-prepared transparent solution had a red–violet colour and showed no sign of precipitates even after weeks of storage. After preparation, the solution was stirred for several hours before deposition to ensure proper mixing.

Thin Film Preparation and Coating: The spin coating process was conducted in a clean room to provide a controlled atmosphere and to avoid comet streaks in the films due to dust particles. Prior to the spin coating, 10 mm x 10 mm x 0.5 mm sapphire (0001) substrates were coated with a 100 nm Pt layer as back electrode using sputter deposition. In the first step, the precursor solution was spin-coated onto the substrates at 3,000 rpm for 45 s. The as-prepared films were heated at 400 °C for 4 min on a hotplate and subsequently cooled down to room temperature. To increase the thickness of the thin film cathodes, the deposition was repeated two additional times. After the final deposition, the films were calcined in an oven at 700 °C for 5 h under atmospheric conditions (10 K min^{-1} heating rate). Afterward, the as-prepared thin film cathodes (Figure S5, Supporting Information) were stored in an Ar glovebox until further use. To investigate the influence of an ultrathin surface coating with varying thickness on the electrochemical performance, NCM samples were coated with a thin Al_2O_3 film using atomic layer deposition (ALD), which enables a homogeneous coating even of porous samples.[66,67,88] The ALD deposition was carried out in a PicoSun R200 ALD reactor using trimethylaluminium (TMA, STREM chemicals inc., min. 98%) as precursor and deionized water as reactant for TMA to form the oxide layer. During deposition, the reactor was kept at 150 °C with an intermediate space flow of 150 sccm nitrogen between reactor and vacuum pump. To access the influence of the coating thickness on the electrochemical performance, different thin films were coated using 20 and 50 ALD cycles, respectively. To determine the Al_2O_3 film thickness, a Si wafer was placed inside the reaction chamber together with each of the NCM thin films serving as a reference. Using X-ray reflectometry (XRR), the thicknesses of the coating layer were determined to be 2 and 5 nm, respectively.

Structural Characterization: Microstructural analysis of the thin film cathodes was done by Raman spectroscopy and grazing incident X-ray diffraction (GIXRD). Raman spectroscopy was carried out using a Leica top-illuminating bright field microscope with a Leica 50 ×/0.75 *NA* objective and a Renishaw InVia spectrometer. Measurements were done at room temperature between 200 and 800 cm^1 with an Arion laser (λ_{laser} = 514.5 nm) and a resolution of 2 cm^1. The laser power never exceeded 5 mW during the measurement. A Panalytical X´Pert Pro MRD with CuK_α radiation (40 kV, 40 mA, $\lambda_{CuK\alpha}$ = 1.542 Å) was used to measure the thin films at an incident beam angle of $\omega = 1$ between $2\Theta =$ 10–90°. For the structural and elemental analysis of the surface, a Zeiss SMT Merlin high-resolution Schottky field-emission scanning electron microscope (HRSEM) equipped with an X-MAX Extreme EDS detector (Oxford Instruments) was utilized. The morphology of the surface was investigated using a Bruker Multimode 8 atomic force microscope (AFM) with a ScanAsyst cantilever and the eponymous modus. From the AFM measurements, the average surface roughness of each sample was determined after the DIN ISO 4287 norm using an average of five different measurements. To confirm the coating of the samples, X-ray photoelectron spectroscopy (XPS) was carried out on a PHI5000 Versa Probe II. The samples were transferred under Ar atmosphere into the XPS system using a transfer vessel. Analysis was performed using a monochromatic Al Kα source ($h\nu$ = 1486.6 eV, 50 W) having a spot diameter of 200 μm. To avoid charging effects, a dual beam charge neutralizer was used. Depth profiles were achieved by using an Ar^+ sputter beam (0.5 kV, 0.5 µA, (2 × 2) μm^2). All spectra were calibrated in relation to the signal of adventitious carbon (284.8 eV).

Electrochemical Characterization: The pristine and coated NCM cathodes were assembled in a pouch bag setup in an Ar filled glovebox ensuring oxygen and water levels below 1 ppm. Metallic lithium was used as a counter and reference electrode, the NCM thin films were used as working electrode. The electrodes were separated by a Whatman glass fibre separator (GFA) soaked with 50 µL of electrolyte. As electrolyte 1 M LiPF6 as conducting salt in EC/DMC (LP30, battery grade, ≤15 ppm, Sigma–Aldrich) was used. Electrochemical analyses were performed using a VMP3 battery cycling systems by Biologic. Before each measurement, the open-circuit potential was recorded for 30 min to ensure equilibrium inside the cell. The galvanostatic cell cycling tests were conducted with upper and lower cutoff voltages of 4.2 V versus Li/Li^+ and 3.0 V versus Li/Li^+. Cyclic voltammetry (CV) measurements were recorded at a scan rate of 0.1 mV s^{-1} in a voltage range between 3.0 and 4.2 V versus Li/Li^+. All electrochemical experiments were carried out at room temperature. For the post-mortem characterization, the electrochemical cells were disassembled, the cathode films were rinsed five times with DMC, and subsequently dried at 60 °C for 18 h.

Supporting Information

Supporting Information is available from the Wiley Online Library or from the author.

Acknowledgements

H.H. and M.T.E. thank the German Federal Ministry of Education and Research (BMBF) for funding of the NanoMatFutur project NiKo (03XP0093) as well as Felix Walther for helping in the interpretation of the XPS measurements.

Open access funding enabled and organized by Projekt DEAL.

Conflict of Interest

The authors declare no conflict of interest.

Data Availability Statement

Research data are not shared.

Keywords

cathode materials, coatings, lithium ion batteries, spin-coating, thin film model systems

Received: November 26, 2020
Revised: February 2, 2021
Published online: March 1, 2021

[1] Y. Ding, R. Wang, L. Wang, K. Cheng, Z. Zhao, D. Mu, B. Wu, *Energy Procedia* **2017**, *105*, 2941.
[2] Y. Ding, D. Mu, B. Wu, R. Wang, Z. Zhao, F. Wu, *Appl. Energy* **2017**, *195*, 586.
[3] A. Manthiram, B. Song, W. Li, *Energy Storage Mater.* **2017**, *6*, 125.
[4] J. Kim, H. Ma, H. Cha, H. Lee, J. Sung, M. Seo, P. Oh, M. Park, J. Cho, *Energy Environ. Sci.* **2018**, *11*, 1449.
[5] K. Mizushima, P. C. Jones, P. J. Wiseman, J. B. Goodenough, *Solid State Ionics* **1981**, *3–4*, 171.
[6] N. Nitta, F. Wu, J. T. Lee, G. Yushin, *Mater. Today* **2015**, *18*, 252.
[7] W. Li, B. Song, A. Manthiram, *Chem. Soc. Rev.* **2017**, *46*, 3006.
[8] E. Markevich, G. Salitra, D. Aurbach, *ACS Energy Lett.* **2017**, *2*, 1337.
[9] K. Edström, T. Gustafsson, J. O. Thomas, *Electrochim. Acta* **2004**, *50*, 397.
[10] N. P. W. Pieczonka, Z. Liu, P. Lu, K. L. Olson, J. Moote, B. R. Powell, J.-H. Kim, *J. Phys. Chem. C* **2013**, *117*, 15947.
[11] C. L. Campion, W. Li, B. L. Lucht, *J. Electrochem. Soc.* **2005**, *152*, A2327.
[12] S. Nowak, M. Winter, *Acc. Chem. Res.* **2018**, *51*, 265.
[13] R. Hausbrand, G. Cherkashinin, H. Ehrenberg, M. Gröting, K. Albe, C. Hess, W. Jaegermann, *Mater. Sci. Eng., B* **2015**, *192*, 3.
[14] L. Baggetto, D. Mohanty, R. A. Meisner, C. A. Bridges, C. Daniel, D. L. Wood, N. J. Dudney, G. M. Veith, *RSC Adv.* **2014**, *4*, 23364.
[15] H. M. K. Sari, X. Li, *Adv. Energy Mater.* **2019**, *9*, 1901597.
[16] K. Tasaki, K. Kanda, S. Nakamura, M. Ue, *J. Electrochem. Soc.* **2003**, *150*, A1628.
[17] S. F. Lux, I. T. Lucas, E. Pollak, S. Passerini, M. Winter, R. Kostecki, *Electrochem. Commun.* **2012**, *14*, 47.
[18] M. Evertz, F. Horsthemke, J. Kasnatscheew, M. Börner, M. Winter, S. Nowak, *J. Power Sources* **2016**, *329*, 364.
[19] M. Lang, M. S. D. Darma, K. Kleiner, L. Riekehr, L. Mereacre, M. Ávila Pérez, V. Liebau, H. Ehrenberg, *J. Power Sources* **2016**, *326*, 397.
[20] A. M. Haregewoin, A. S. Wotango, B. Hwang, *Energy Environ. Sci.* **2016**, *9*, 1955.
[21] T. He, Y. Lu, Y. Su, L. Bao, J. Tan, L. Chen, Q. Zhang, W. Li, S. Chen, F. Wu, *ChemSusChem* **2018**, *11*, 1639.
[22] C. C. Wang, A. Manthiram, *J. Mater. Chem. A* **2013**, *1*, 10209.
[23] C. Qin, J. Cao, J. Chen, G. Dai, T. Wu, Y. Chen, Y. Tang, A. Li, Y. Chen, *Dalton Trans.* **2016**, *45*, 9669.
[24] Z. Chen, D. Chao, J. Lin, Z. Shen, *Mater. Res. Bull.* **2017**, *96*, 491.
[25] R. S. Negi, S. P. Culver, A. Mazilkin, T. Brezesinski, M. T. Elm, *ACS Appl. Mater. Interfaces* **2020**, *12*, 31392.
[26] S. T. Myung, K. Izumi, S. Komaba, Y. K. Sun, H. Yashiro, N. Kumagai, *Chem. Mater.* **2005**, *17*, 3695.
[27] H.-M. Cho, M. V. Chen, A. C. MacRae, Y. S. Meng, *ACS Appl. Mater. Interfaces* **2015**, *7*, 16231.
[28] W. Cho, S. M. Kim, J. H. Song, T. Yim, S. G. Woo, K. W. Lee, J. S. Kim, Y. J. Kim, *J. Power Sources* **2015**, *282*, 45.
[29] J. Cho, Y. J. Kim, B. Park, *Chem. Mater.* **2000**, *12*, 3788.
[30] D. Wang, X. Li, Z. Wang, H. Guo, Y. Xu, Y. Fan, *Electrochim. Acta* **2016**, *196*, 101.
[31] D. Zuo, G. Tian, X. Li, D. Chen, K. Shu, *J. Alloys Compd.* **2017**, *706*, 24.
[32] W. Sun, M. Xie, X. Shi, L. Zhang, *Mater. Res. Bull.* **2015**, *61*, 287.
[33] M. R. Laskar, D. H. K. Jackson, S. Xu, R. J. Hamers, D. Morgan, T. F. Kuech, *ACS Appl. Mater. Interfaces* **2017**, *9*, 11231.
[34] C. Jacob, T. Lynch, A. Chen, J. Jian, H. Wang, *J. Power Sources* **2013**, *241*, 410.
[35] J. B. Bates, N. J. Dudney, B. J. Neudecker, F. X. Hart, H. P. Jun, S. A. Hackney, *J. Electrochem. Soc.* **2000**, *147*, 59.
[36] P. J. Bouwman, B. A. Boukamp, H. J. M. Bouwmeester, H. J. Wondergem, *J. Electrochem. Soc.* **2001**, *4*, A311.
[37] H. Xia, L. Lu, G. Ceder, *J. Power Sources* **2006**, *159*, 1422.
[38] T. Kwon, T. Ohnishi, K. Mitsuishi, T. C. Ozawa, K. Takada, *J. Power Sources* **2015**, *274*, 417.
[39] B. Yan, J. Liu, B. Song, P. Xiao, L. Lu, *Sci. Rep.* **2013**, *3*, 3332.
[40] M. Strafela, H. Leiste, K. Seemann, H. J. Seifert, S. Ulrich, *Vacuum* **2016**, *131*, 240.
[41] N. D. Phillip, R. E. Ruther, X. Sang, Y. Wang, R. R. Unocic, A. S. Westover, C. Daniel, G. M. Veith, *ACS Appl. Energy Mater.* **2019**, *2*, 1405.
[42] R. Ruess, S. Schweidler, H. Hemmelmann, G. Conforto, A. Bielefeld, D. A. Weber, J. Sann, M. T. Elm, J. Janek, *J. Electrochem. Soc.* **2020**, *167*, 100532.
[43] K. M. Shaju, G. V. Subba Rao, B. V. R. Chowdari, *Electrochim. Acta* **2002**, *48*, 145.
[44] T. H. Cho, S. M. Park, M. Yoshio, T. Hirai, Y. Hideshima, *J. Power Sources* **2005**, *142*, 306.
[45] J. Maibach, F. Lindgren, H. Eriksson, K. Edström, M. Hahlin, *J. Phys. Chem. Lett.* **2016**, *7*, 1775.
[46] T. Hagio, A. Takase, S. Umebayashi, *J. Mater. Sci. Lett.* **1992**, *11*, 878.
[47] B. J. Tan, K. J. Klabunde, P. M. A. Sherwood, *Chem. Mater.* **1990**, *2*, 186.
[48] A. M. Andersson, D. P. Abraham, R. Haasch, S. MacLaren, J. Liu, K. Amine, *J. Electrochem. Soc.* **2002**, *149*, A1358.
[49] R. Azmi, V. Trouillet, M. Strafela, S. Ulrich, H. Ehrenberg, M. Bruns, *Surf. Interface Anal.* **2018**, *50*, 43.
[50] W. Liu, X. Li, D. Xiong, Y. Hao, J. Li, H. Kou, B. Yan, D. Li, S. Lu, A. Koo, K. Adair, X. Sun, *Nano Energy* **2018**, *44*, 111.
[51] J. Chen, H. Yang, T. Li, C. Liu, H. Tong, J. Chen, Z. Liu, L. Xia, Z. Chen, J. Duan, L. Li, *Front. Chem.* **2019**, *7*, 500.
[52] D. Mohanty, K. Dahlberg, D. M. King, L. A. David, A. S. Sefat, D. L. Wood, C. Daniel, S. Dhar, V. Mahajan, M. Lee, F. Albano, *Sci. Rep.* **2016**, *6*, 26532.
[53] A. Yano, S. Aoyama, M. Shikano, H. Sakaebe, K. Tatsumi, Z. Ogumi, *J. Electrochem. Soc.* **2015**, *162*, A3137.
[54] J. W. Kim, J. J. Travis, E. Hu, K. W. Nam, S. C. Kim, C. S. Kang, J. H. Woo, X. Q. Yang, S. M. George, K. H. Oh, S. J. Cho, S. H. Lee, *J. Power Sources* **2014**, *254*, 190.
[55] J. Kasnatscheew, M. Evertz, B. Streipert, R. Wagner, R. Klöpsch, B. Vortmann, H. Hahn, S. Nowak, M. Amereller, A. C. Gentschev, P. Lamp, M. Winter, *Phys. Chem. Chem. Phys.* **2016**, *18*, 3956.
[56] M. M. Doeff, In *Batteries for Sustainability*, (Ed.: R. J. Brodd), Springer Science + Business Media, New York **2013**, pp. 5–49.
[57] D. Guan, J. A. Jeevarajan, Y. Wang, *Nanoscale* **2011**, *3*, 1465.
[58] Y. Huang, J. Chen, F. Cheng, W. Wan, W. Liu, H. Zhou, X. Zhang, *J. Power Sources* **2010**, *195*, 8267.
[59] B. Han, T. Paulauskas, B. Key, C. Peebles, J. S. Park, R. F. Klie, J. T. Vaughey, F. Dogan, *ACS Appl. Mater. Interfaces* **2017**, *9*, 14769.
[60] X. Zhang, W. J. Jiang, A. Mauger, F. G. Qilu, C. M. Julien, *J. Power Sources* **2010**, *195*, 1292.
[61] X. Cao, *Int. J. Electrochem. Sci.* **2016**, *11*, 5267.
[62] P. Lanz, C. Villevieille, P. Novák, *Electrochim. Acta* **2014**, *130*, 206.
[63] C. L. Liao, Y. H. Lee, K. Z. Fung, *J. Alloys Compd.* **2007**, *436*, 303.
[64] M. Kerlau, M. Marcinek, V. Srinivasan, R. M. Kostecki, *Electrochim. Acta* **2007**, *52*, 5422.
[65] E. Flores, P. Novák, E. J. Berg, *Front. Energy Res.* **2018**, *6*, 82.
[66] M. F. Zscherp, J. Glaser, C. Becker, A. Beyer, P. Cop, J. Schörmann, K. Volz, M. T. Elm, *Cryst. Growth Des.* **2020**, *20*, 2194.

[67] P. Cop, E. Celik, K. Hess, Y. Moryson, P. Klement, M. T. Elm, B. M. Smarsly, *ACS Appl. Nano Mater.* **2020**, *3*, 10757.
[68] C. Detavernier, J. Dendooven, S. P. Sree, K. F. Ludwig, J. a Martens, *Chem. Soc. Rev.* **2011**, *40*, 5242.
[69] M. Strafela, H. Leiste, K. Seemann, H. J. Seifert, S. Ulrich, *Vacuum* **2016**, *131*, 240.
[70] H. Xia, L. Lu, G. Ceder, *J. Alloys Compd.* **2006**, *417*, 304.
[71] V. I. Nefedov, Y. A. Buslaev, Y. V. Kokunov, *Zh. Neorg. Khim.* **1974**, *19*, 1166.
[72] W. E. Morgan, J. R. Van Wazer, W. J. Stec, *J. Am. Chem. Soc.* **1973**, *95*, 751.
[73] J. F. Moulder, W. F. Stickle, P. E. Sobol, K. D. Bomben, *Handbook of X-Ray Photoelectron Spectroscopy*, (Ed.: J. Chastain), 1st ed., Perkin-Elmer Corporation, Eden Prairie **1992**.
[74] S. W. Gaarenstroom, N. Winograd, *J. Chem. Phys.* **1977**, *67*, 3500.
[75] K. Rui, Z. Wen, Y. Lu, J. Jin, C. Shen, *Adv. Energy Mater.* **2015**, *5*, 1401716.
[76] Y. Lu, Y. P. Zhou, Q. Y. Yan, E. Fong, *J. Mater. Chem. A* **2016**, *4*, 2691.
[77] Y. S. Lee, *J. Fluorine Chem.* **2007**, *128*, 392.
[78] W. Li, A. Dolocan, P. Oh, H. Celio, S. Park, J. Cho, A. Manthiram, *Nat. Commun.* **2017**, *8*, 1.
[79] H. Nara, K. Morita, T. Yokoshima, D. Mukoyama, T. Momma, T. Osaka, *AIMS Mater. Sci.* **2016**, *3*, 448.
[80] D. R. Gallus, R. Schmitz, R. Wagner, B. Hoffmann, S. Nowak, I. Cekic-Laskovic, R. W. Schmitz, M. Winter, *Electrochim. Acta* **2014**, *134*, 393.
[81] H. Zheng, Q. Sun, G. Liu, X. Song, V. S. Battaglia, *J. Power Sources* **2012**, *207*, 134.
[82] A. Martens, C. Bolli, A. Hoffmann, C. Erk, T. Ludwig, M. E.l Kazzi, U. Breddemann, P. Novák, I. Krossing, *J. Electrochem. Soc.* **2020**, *167*, 070510.
[83] D. S. Hall, R. Gauthier, A. Eldesoky, V. S. Murray, J. R. Dahn, *ACS Appl. Mater. Interfaces* **2019**, *11*, 14095.
[84] S. Hong, B. Hong, W. Song, Z. Qin, B. Duan, Y. Lai, F. Jiang, *J. Electrochem. Soc.* **2018**, *165*, A368.
[85] Q. Q. Liu, L. Ma, C. Y. Du, J. R. Dahn, *Electrochim. Acta* **2018**, *263*, 237.
[86] C. Wang, L. Yu, W. Fan, J. Liu, L. Ouyang, L. Yang, M. Zhu, *ACS Appl. Energy Mater.* **2018**, *1*, 2647.
[87] W. Zhao, G. Zheng, M. Lin, W. Zhao, D. Li, X. Guan, Y. Ji, G. F. Ortiz, Y. Yang, *J. Power Sources* **2018**, *380*, 149.
[88] E. Celik, R. S. Negi, M. Bastianello, D. Boll, A. Mazilkin, T. Brezesinski, M. T. Elm, *Phys. Chem. Chem. Phys.* **2020**, *22*, 11519.